J. Fluid Mech. (1996), *vol.* 310, *pp.* 269–292

Topology of fine-scale motions in turbulent channel flow

By HUGH M. BLACKBURN[1]†, NAGI N. MANSOUR[2] AND BRIAN J. CANTWELL[3]

[1]Department of Mechanical Engineering, Monash University, Clayton, Vic 3168, Australia
[2]NASA Ames Research Center, Mail Stop 202A-1, Moffett Field, CA 94035, USA
[3]Department of Aeronautics and Astronautics, Stanford University, Stanford, CA 94305, USA

(Received 21 July 1993 and in revised form 6 September 1995)

An investigation of topological features of the velocity gradient field of turbulent channel flow has been carried out using results from a direct numerical simulation for which the Reynolds number based on the channel half-width and the centreline velocity was 7860. Plots of the joint probability density functions of the invariants of the rate of strain and velocity gradient tensors indicated that away from the wall region, the fine-scale motions in the flow have many characteristics in common with a variety of other turbulent and transitional flows: the intermediate principal strain rate tended to be positive at sites of high viscous dissipation of kinetic energy, while the invariants of the velocity gradient tensor showed that a preference existed for stable focus/stretching and unstable node/saddle/saddle topologies. Visualization of regions in the flow with stable focus/stretching topologies revealed arrays of discrete downstream-leaning flow structures which originated near the wall and penetrated into the outer region of the flow. In all regions of the flow, there was a strong preference for the vorticity to be aligned with the intermediate principal strain rate direction, with the effect increasing near the walls in response to boundary conditions.

1. Introduction

Turbulence modelling remains the major challenge in our ability to predict turbulent flows. Model development has been slow because it seems that different models are needed for different flows, as the large-scale features of the turbulence appear to be flow-dependent. A major motivation for the development of large-eddy simulations has been the belief that although large structures may vary from flow to flow, at smaller scales the features should be less flow-dependent and more amenable to modelling. This belief in the fine-scale universality of turbulent flows is supported by evidence from recent investigations, as outlined below. Universal fine-scale features, if they can be identified, should potentially be of greater utility in construction of subgrid-scale models than assumptions concerning statistical isotropy of turbulent fluctuations at high wavenumbers.

A number of recent studies of the properties of the velocity gradient and rate of strain fields from direct numerical simulations of turbulent and transitional flows have produced results which indicate a number of common features of the fine-scale

† Current address: CSIRO, Division of Building, Construction and Engineering, PO Box 56, Highett, Vic 3190, Australia.

motions in a variety of flow geometries, despite different large-scale motions. Authors have typically presented combinations of statistical analyses and flow visualizations based on one or more realizations from the simulations.

Ashurst *et al.* (1987) studied a simulated incompressible isotropic turbulent flow with Taylor microscale Reynolds number $Re_\lambda = 83$ and a homogeneous incompressible shear flow with similar Reynolds number. The isotropic flow was forced into a state of statistical equilibrium ('driven') by adding energy at low wavenumbers. In both flows, they found that on average the intermediate principal strain rate tended to have a positive value which increased as the local viscous kinetic energy dissipation rate on which the sample was conditioned rose, with the ratios of principal strain rates λ_1, λ_2, λ_3 approaching 3:1:−4 at higher conditioning levels. In addition, they found that the vorticity $\boldsymbol{\omega}$ tended to align with the intermediate principal strain rate direction $\boldsymbol{e}_2$, based on a study of the probability density function (PDF) of the cosine of the angle between their directions.

Vincent & Meneguzzi (1991) studied a simulation of driven isotropic turbulence with $Re_\lambda \simeq 150$. Again, the intermediate principal strain rate was positive at approximately two-thirds of the grid points. Vortex 'tubes' were observed, with a typical diameter intermediate between the Kolmogorov and Taylor microscales and length of the order of the integral scale of the flow (similar observations have been published by She, Jackson & Orszag 1990). The highest rates of strain in the flow were seen in the vicinity of the vortex tubes, with the eigenvectors of the most positive and negative principal strain rates ($\boldsymbol{e}_1$ and $\boldsymbol{e}_3$) perpendicular to the vorticity which thus tended to align with the intermediate principal strain rate direction $\boldsymbol{e}_2$. Vortex tubes were also observed by Ruetsch & Maxey (1991) in results from a simulation of driven isotropic turbulence with $Re_\lambda \simeq 60$. In a study of sites of kinetic energy dissipation in the flow, they found that the bulk of the dissipation occurred in regions of moderate dissipation which surrounded the vortex tubes and that the most intense dissipation was observed between tubes where the induced strain rate fields of the tubes overlapped. In a more recent paper, Vincent & Meneguzzi (1994) reported that most vortex tubes found in their simulation of homogeneous turbulence evolved from shear layers by an instability mechanism, during the influence of transverse straining. The sites of highest dissipation were in the vicinity of, but outside, vorticity tube cores. In a study of alignment properties in a simulation of decaying homogeneous turbulence, Vincent & Meneguzzi found that the tendency for alignment of the vorticity with the intermediate principal rate of strain direction occurred before the roll-up of the vortex sheets into tubes.

In a study of transitional Reynolds number inhomogeneous shear flows, Chen *et al.* (1990) presented results from simulations of time-developing compressible and incompressible mixing layers with Reynolds numbers (based on the velocity difference and the initial vorticity thickness) of 1600 and 3000 respectively. Chen *et al.* introduced the use of flow visualization based on classification of local flow topologies and demonstrated that for the mixing layers there was a correspondence between visualization based on physical quantities such as enstrophy on the one hand, and on topological classification on the other. Examination of scatter plots of the second and third invariants of the rate of strain tensor showed that the intermediate principal strain rate again tended to be positive, especially when the local rate of turbulent kinetic energy dissipation was high. Flow visualization showed that regions of high enstrophy and high dissipation tended to be associated in these flows, although the incompressible mixing layer contained streamwise counter-rotating vortices with high enstrophy but relatively low dissipation. The work of

Sondergaard *et al.* (1991) extended the range of flows to include time-developing compressible and incompressible plane wakes with Reynolds numbers of 300 and 500; the two additional flows also showed a tendency for the intermediate principal strain rate to be positive where dissipation was high. In that paper, properties of the local alignment between the vorticity vector and the principal rate of strain directions for the mixing layers were studied and it was shown that the vorticity tended to align with the intermediate principal strain rate direction at sites of high dissipation. Scatter plots of the second and third invariants of the velocity gradient tensor showed that of the four possible local flow topologies there tended to be a preference for stable focus/stretching and unstable node/saddle/saddle in all the flows (we present a more extensive discussion of tensor invariants and flow topologies below). Soria *et al.* (1994) studied the topology of plane mixing layers computed from laminar as well as turbulent initial conditions. They found that virtually all of the dissipation was accomplished by intermediate- and fine-scale motions characterized by two positive principal rates of strain.

Finally we mention the experimentally based study of Tsinober, Kit & Dracos (1992), where results for alignment effects in grid-generated and boundary layer turbulence were presented. In both cases the propensity for alignment between the vorticity and the intermediate rate of strain eigenvector was observed. As in the studies of Ashurst *et al.* (1987) and Vincent & Meneguzzi (1994), this conclusion was based on an examination of the PDFs of the cosines of the angles between the vorticity and the principal strain rate directions.

The picture which has begun to emerge from these studies is that for a variety of turbulent and transitional flows with differing large-scale structure, much of the kinetic energy dissipation occurs in regions which surround elongated structures with high enstrophy. In all cases for which alignment results have been presented, it has been found that the vorticity $\boldsymbol{\omega}$ tends to align with the intermediate principal strain rate direction $\boldsymbol{e}_2$. In addition, the intermediate principal strain rate λ_2 is positive on average. Jimenez (1992) suggested a kinematic model which would indicate that this strain–vorticity geometry should occur in the neighbourhood of a local maximum of vorticity and Burgers' stretched vortex solution was used to illustrate the point. Although this model describes a flow situation in which the observed geometry can occur it does not explain the tendency for turbulent flows to evolve to such a state. The observed preference for two of four possible local flow topologies in the fine-scale motions of inhomogeneous shear flows remains unexplained and it is unknown if this preference is common to other flows or at higher Reynolds numbers.

In this paper, we examine results from one realization of a direct numerical simulation of an incompressible turbulent channel flow with Reynolds number based on the centreline mean flow speed and the channel half-width of 7860. This expands the range of flow types to include situations in which the presence of a wall has an effect. In addition, flow visualization based on topological classification of the velocity gradient tensor has been used to examine features of the turbulent boundary layer.

2. Classification of local flow topology

The flow pattern at each point in the flow may be assessed from the viewpoint of an observer travelling with the local velocity of the flow. For such an observer, each point is a critical point (that is, the local streamlines have indeterminate slope) and the topology can be categorized using critical point terminology (Perry & Chong 1987).

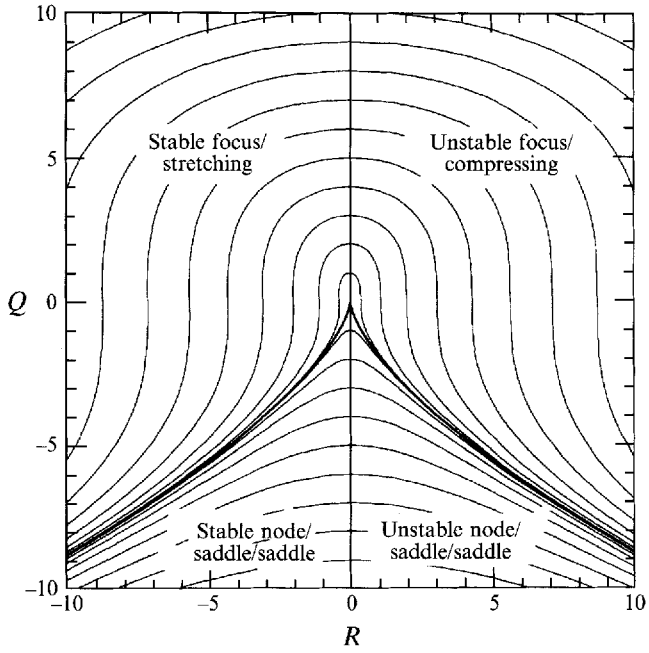

FIGURE 1. Plot showing the space of tensor invariants Q and R for incompressible flow, with lines corresponding to constant values of the discriminant $D = (27/4)R^2 + Q^3$. The different regions are labelled according to the terminology of Chong *et al.* (1990).

2.1. *Invariants of the velocity gradient tensor and flow topology*

The velocity gradient tensor $\boldsymbol{A} = \nabla \boldsymbol{u}$ with Cartesian components $A_{ij} = \partial u_j/\partial x_i$ may be decomposed into the symmetric rate of strain tensor $\boldsymbol{S}$ with Cartesian components $S_{ij} = (A_{ij} + A_{ji})/2$ and the skew-symmetric rate of rotation tensor $\boldsymbol{\Omega}$ with components $\Omega_{ij} = (A_{ij} - A_{ji})/2$. The eigenvalues Λ of $\boldsymbol{A}$ are obtained as solutions of the characteristic equation

$$\Lambda^3 + P\Lambda^2 + Q\Lambda + R = 0, \tag{2.1}$$

with the tensor invariants P, Q and R given by

$$P = -S_{ii} = -\mathrm{tr}(\boldsymbol{A}) \quad (= 0 \text{ for incompressible flow}), \tag{2.2a}$$

$$Q = \tfrac{1}{2}(P^2 - S_{ij}S_{ji} - \Omega_{ij}\Omega_{ji}) = \tfrac{1}{2}\left\{[\mathrm{tr}(\boldsymbol{A})]^2 - \mathrm{tr}(\boldsymbol{A}^2)\right\}, \tag{2.2b}$$

$$R = \tfrac{1}{3}(-P^3 + 3PQ - S_{ij}S_{jk}S_{ki} - 3\Omega_{ij}\Omega_{jk}S_{ki}) = -\det(\boldsymbol{A}). \tag{2.2c}$$

The topological features of the velocity gradient tensor as a function of position in (P,Q,R) space have been detailed by Chong, Perry & Cantwell (1990). The surface given by

$$27R^2 + (4P^3 - 18PQ)R + (4Q^3 - P^2Q^2) = 0 \tag{2.3}$$

divides the space of the invariants into two regions, one where Λ takes one real, two complex-conjugate values, the other with three real distinct eigenvalues.

For the $P = 0$ plane to which the rate of strain tensors for incompressible flows are restricted, the value of the discriminant

$$D = (27/4)R^2 + Q^3 \tag{2.4}$$

determines the nature of the eigenvalues of $\boldsymbol{A}$. $D > 0$ gives rise to one real, two complex-conjugate eigenvalues; $D < 0$ gives the three real, distinct values, while on

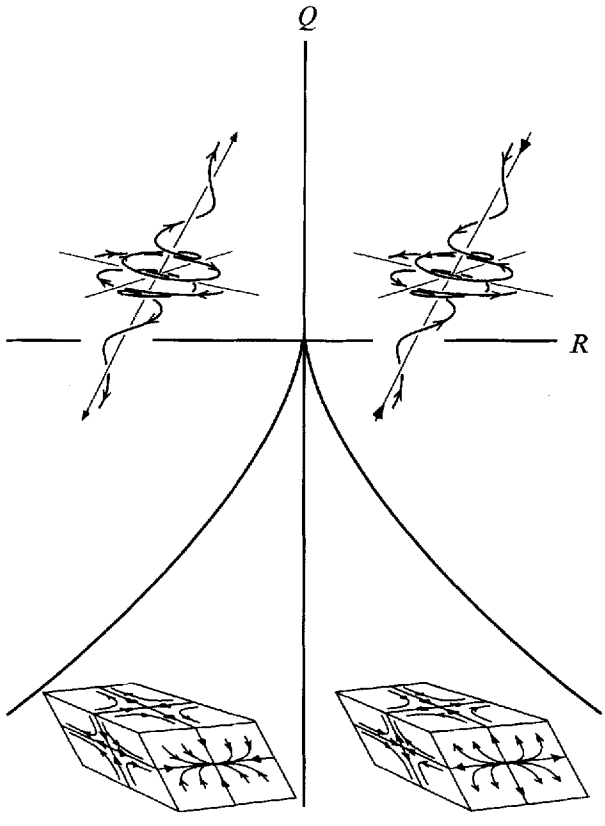

FIGURE 2. Local flow fields (streamlines) for an observer travelling with the fluid for the topological classifications: upper left, stable focus/stretching; upper right, unstable focus/compressing; lower left, stable node/saddle/saddle; lower right, unstable node/saddle/saddle.

the lines $R = \pm(2\sqrt{3}/9)(-Q)^{3/2}$ for which $D = 0$ there are three real eigenvalues of which two are equal. A further classification is made according to the sign of R; in the left half of the (Q,R) plane the real parts of the complex-conjugate eigenvalues or two of the three real eigenvalues are negative and the critical points of the flow are classified as stable, while in the right half-plane the real parts of the complex-conjugate or two of the three real eigenvalues are positive and the critical points are classified as unstable, following standard terminology. A diagram of the (Q,R)-plane for which $P = 0$ is shown in figure 1, with labels for the various classifications.

In the terminology of Chong *et al.*, critical point topologies which fall in the upper left-hand region of the plane are called stable focus/stretching, the upper right-hand region unstable focus/compressing, those in the lower left-hand region stable node/saddle/saddle and those in the lower right-hand region unstable node/saddle/saddle. The shapes of the local flow fields corresponding to these topologies (the local flow pattern which would be seen by an observer travelling with a fluid particle) are indicated in figure 2.

2.2. *Invariants of the rate of strain tensor*

The local topology of any second-order tensor field may be classified in the same way. In the following, we also discuss the topological features of the local rate of strain tensor $\boldsymbol{S}$ in terms of its invariants R_s and Q_s ($P_s = P = 0$ due to incompressibility).

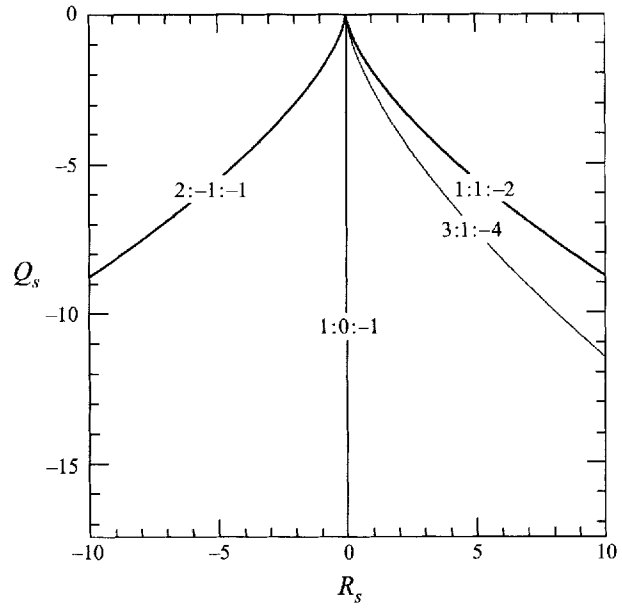

FIGURE 3. Lines in (Q_s,R_s)-space corresponding to different ratios of principal strains $\lambda_1:\lambda_2:\lambda_3$. All Q_s,R_s pairs must fall below the lines corresponding to the ratios 2:−1:−1 and 1:1:−2 as a consequence of the symmetry of $\boldsymbol{S}$.

For this symmetric tensor,

$$Q_s = -\tfrac{1}{2}S_{ij}S_{ji} = -\tfrac{1}{2}\mathrm{tr}(\boldsymbol{S}^2), \tag{2.5a}$$

$$R_s = -\tfrac{1}{3}S_{ij}S_{jk}S_{ki} = -\tfrac{1}{3}\mathrm{tr}(\boldsymbol{S}^3). \tag{2.5b}$$

Owing to the symmetry of $\boldsymbol{S}$ all eigenvalues must be real, hence in the (R_s,Q_s)-plane only classifications for which $D_s = (27/4)R_s^2 + Q_s^3 \leqslant 0$ can be obtained. Since the ratios of the principal rates of strain (eigenvalues of $\boldsymbol{S}$; λ_1, λ_2, λ_3 in descending order) will be discussed, we remark here that each set of ratios corresponds to a line in the R_s–Q_s plane. If $a = \lambda_2/\lambda_1$ then

$$R_s = (-Q_s)^{3/2}a(1+a)(1+a+a^2)^{-3/2} \tag{2.6}$$

(note that $Q_s \leqslant 0$). Curves corresponding to the principal strain rate ratios $\lambda_1:\lambda_2:\lambda_3$; 1:1:−2, 3:1:−4, 1:0:−1 and 2:−1:−1 are shown in figure 3. Note also that Q_s is proportional to the local rate of kinetic energy dissipation: $\phi = 2\nu S_{ij}S_{ji} = -4\nu Q_s$, so that regions with large negative values of Q_s are sites of high dissipation. Finally, the three principal rate of strain directions are orthogonal, again owing to the symmetry of $\boldsymbol{S}$.

Classical scaling arguments presented by Chen *et al.* (1990) imply that fluctuating velocity gradients scale with the square-root of mean flow Reynolds numbers so that Q_s scales with Re and R_s with $Re^{3/2}$; since the range of length scales of motion in turbulent flows increases with Reynolds number, fine-scale motion can be said to correspond to points far from the origin in (Q_s,R_s) space.

2.3. *Relative importance of rates of strain and rotation*

The second invariant of $\boldsymbol{A}$, Q, is a measure of the relative importance of the straining and rotational parts of the velocity gradient tensor: where Q is large and positive, the

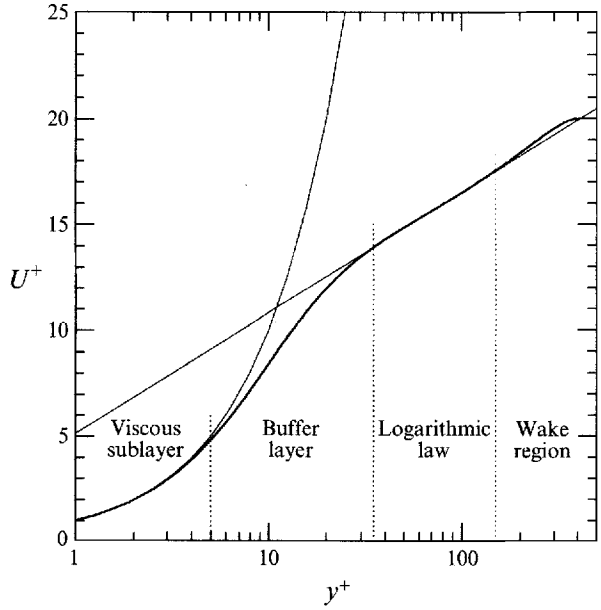

FIGURE 4. Mean velocity profile for the channel flow. The logarithmic-law region is fitted by the equation $U^+ = 5.136 + 0.4053^{-1} \ln y^+$.

enstrophy (square of the vorticity magnitude, twice the second invariant of the rate of rotation tensor Q_Ω) $-\Omega_{ij}\Omega_{ji}$ is large and dominates the strain rate (as expressed by $S_{ij}S_{ji}$ or $-2Q_s$); where Q is large and negative the reverse is true. This relative importance may be expressed graphically by plotting $S_{ij}S_{ji}$ against $-\Omega_{ij}\Omega_{ji}$. Points which lie near the $-\Omega_{ij}\Omega_{ji}$-axis are in nearly pure solid-body rotation, points which lie near the $S_{ij}S_{ji}$-axis have motions which are nearly pure straining, while 'sheet-like' motions where strain rate and rotation are of the same magnitude (e.g. boundary layer mean flow) map to points near the 45° line where $-\Omega_{ij}\Omega_{ji} = S_{ij}S_{ji}$. See Soria *et al.* (1994), figure 3.

3. Data set

The data set used for this investigation was one realization (time step) from a direct numerical simulation of a turbulent channel flow by John Kim (1990, private communication). The Reynolds number based on the semi-channel width (δ) and the mean centreline flow speed $\overline{U}_c$, $Re_\delta = 7860$, while that based on δ and the friction velocity ($u_\tau^2 = \nu \partial U/\partial y|_{wall}$), $Re_\tau = 395$. The dimensions of the channel were $x \times y \times z = 2\pi\delta \times 2\delta \times \pi\delta$ or $2482 \times 790 \times 1241$ in wall units (ν/u_τ).

The mean velocity, obtained from a number of realizations, displayed a typical well-developed turbulent profile with a distinct log-law region, as shown in figure 4, where the normal coordinate is given in wall units and the mean velocity is normalized with the friction velocity: $U^+ = U/u_\tau$. A curve fit for the log-law region ($35 \leqslant y^+ \leqslant 150$) gave

$$U^+ = 5.136 + \frac{1}{0.4053} \ln y^+. \tag{3.1}$$

The numerical method used was the same as that employed by Kim, Moin & Moser (1987), with spatial derivatives obtained from Fourier expansions in the streamwise

(x) and spanwise (z) directions and Chebyshev expansions in the normal (y) direction (the derivatives used here were also obtained spectrally). A larger number of grid points was used in the present simulation, $256 \times 193 \times 192$ in the x-, y- and z-directions respectively, giving a total of approximately 9.5 million points.

The simulation data base from which the present data set was drawn has been examined in a number of previous papers (Kim 1989; Antonia, Kim & Browne 1991; Antonia *et al.* 1992; Rodi & Mansour 1993; Kim & Antonia 1993). In particular, Antonia *et al.* (1992) presented comparisons between statistics compiled from the data base and those derived from laboratory data. While there were no experimental results specifically for $Re_\tau = 395$, the statistics presented (distributions of longitudinal and normal turbulence intensities, Reynolds shear stress, turbulent energy production) for the simulation fell between experimentally derived curves for lower and higher Reynolds numbers (see figures 4, 5, 8 and 11 of the paper).

Ensemble-average statistics were compiled from the data base and examined in the context of k–ϵ modelling by Rodi & Mansour (1993). There, the fields for $Re_\tau = 395$ were analysed for resolution. It was found that the ϵ budget was slightly unbalanced near the wall ($y^+ < 5$). This slight imbalance is unlikely to have significantly affected the results presented herein. When the terms in the ϵ budget were examined in spectral space it was found that all the terms were well resolved (a decay of two orders of magnitude in the coefficients). The lack of balance was due to the term $\langle(\partial^2 u_i'/\partial x_j \partial x_k)(\partial^2 u_i'/\partial x_j \partial x_k)\rangle$ which involves the second derivatives of the (fluctuating) velocity. In this case the coefficients dropped two orders of magnitude but more slowly than the other budget terms. Antonia *et al.* (1992, p. 584) have also discussed detailed resolution studies for results in the data base.

Zang (1991) has raised concern about the degree of resolution required in boundary layer simulations and it seems likely that the extreme near-wall resolution discussed in his article is required to accurately capture the details of transitional flows with spanwise-symmetric initial perturbations. The simulation of transition, however, is significantly different from the simulation of a developed turbulent flow, in which there are continuous, large-amplitude, temporally and spatially random disturbances. In a simulation of transition with imposed symmetry, vortex structures that arise through instability are stretched for very long periods of time, leading to very high gradients. In a turbulent simulation the probability of such lengthy periods of stretching being applied to a particular vortex structure is extremely low. The asymmetry present in developed wall turbulence acts to quickly reduce the spanwise and wall-normal gradients which require such high resolution in symmetric simulations of transition. This probably accounts for the apparent discrepancy between Zang's findings with regard to resolution requirements in transitional flows and those required in direct numerical simulation of developed turbulence.

To conclude discussion of resolution in the present data set, we present in figure 5 a plot of contours of the streamwise component of vorticity near the wall at a section of the flow. The smoothness of the contours at mesh length scales in this case is significant because in the spectral computational scheme used for the simulations, a lack of spatial resolution tends to show up as oscillatory behaviour on the length scale of the mesh. This is due to the low numerical diffusion of the method. Oscillatory behaviour tends to be emphasized in plots of higher-order quantities such as vorticity; examples of the oscillatory behaviour of under-resolved spectral schemes applied to boundary layer transition appear in Zang, Krist & Hussaini (1989). On the other hand, mesh-scale smoothness is not necessarily significant for low-order numerical schemes that are under-resolved, where smoothness may be due to inherent numerical diffusivity.

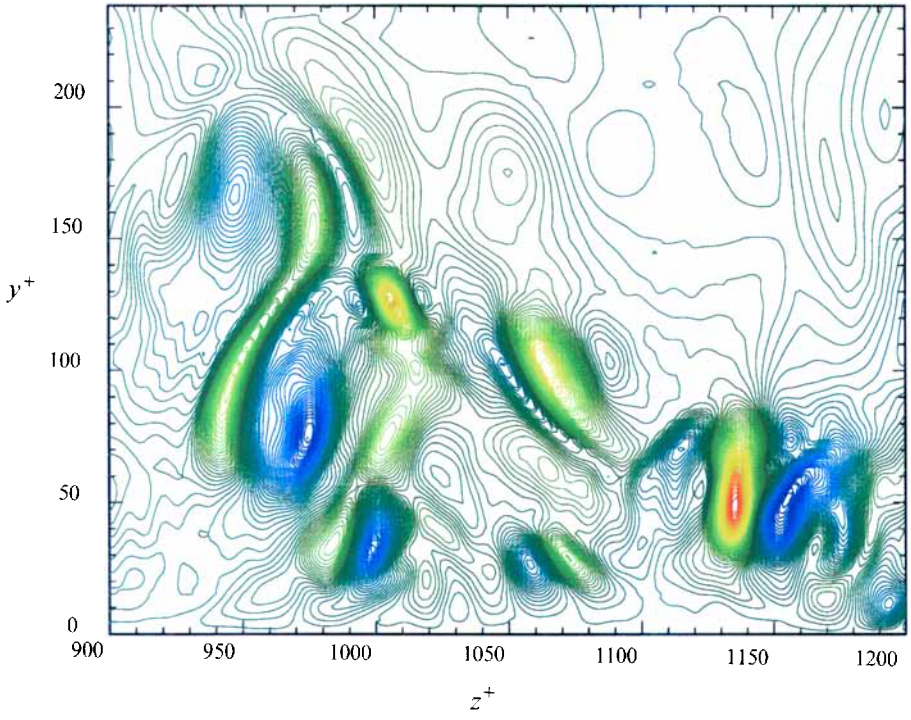

FIGURE 5. Contours of the streamwise component of vorticity near the wall for one plane taken from the data set. Computational mesh shown for comparison.

It should be noted that the results considered in the present paper describe the flow topology near the wall but not at the wall. In order to resolve the topology at the wall a second-order expansion of the velocity field is required which in turn requires numerical computation of higher-order derivatives which may be computed from the present simulation data, but we have not yet carried out such a study. A discussion of the expansion process and the constraints on the invariants of the higher-order field can be found in Chong *et al.* (1990).

In parts of the following discourse, data will be presented in four groups, based on standard terminology: viscous sublayer ($0 \leqslant y^+ \leqslant 5$), buffer layer ($5 \leqslant y^+ \leqslant 35$), logarithmic-law ($35 \leqslant y^+ \leqslant 150$) and wake ($150 \leqslant y^+ \leqslant 395$) regions; these are also indicated in figure 4.

4. Results: joint probability density plots of tensor invariants

The approach taken in this section was to compute the second and third invariants of the velocity gradient and rate of strain tensors at each grid point in the flow, then use the results to prepare approximations to the joint PDFs of the invariants. In addition, values of $S_{ij}S_{ji}$ and $-\Omega_{ij}\Omega_{ji}$ were generated and used to prepare joint PDF estimates. The velocity gradient tensor $\boldsymbol{A}$ was normalized by $\overline{U}_c/\delta$ prior to preparation of the plots so that all quantities are shown in dimensionless form. The results are shown in figure 6 (one graph of each kind has been prepared in each of the four regions of the flow). The aspect ratio in each set of plots has been kept the same but the scales changed to reflect the change in magnitude of the plotted quantities in the four regions of the flow. Since the relative frequencies in the approximations to the joint PDFs were computed over all the grid points in each region without

correction for grid spacing, it should be noted that more weight is given to points closer to the walls as a result of the cosinusoidal y-direction spacing of collocation points demanded by the Chebyshev expansions used in the wall-to-wall direction. The plots show half-decade contours of relative frequency over a four-decade range.

Turning first to the plots of Q *vs.* R, note that for this flow the values of Q and R for the *mean* flow are identically zero everywhere, so that any deviation is a consequence of turbulent fluctuations. As an indication of the rapid growth and subsequent slower decay in the magnitudes of Q and R moving away from the wall, we present in figure 7 a plot of the 90th percentile of Q in each y-plane as a function of y^+ for the single realization analysed. Study of the y-plane-mean values of Q and R showed they stayed close to zero throughout the flow, as expected.

In the plots of Q *vs.* R (figure 6*a–d*), all topologies are observed, but outside the viscous sublayer a preference for the second and fourth quadrants is apparent, indicating preference for stable focus/stretching and unstable node/saddle/saddle topologies. This preference was previously observed in inhomogeneous shear flows (Chen *et al.* 1990; Sondergaard *et al.* 1991; Soria *et al.* 1994). Moving away from the wall, the preference for the second and fourth quadrants became somewhat more apparent, while the magnitudes of the invariants decreased in accordance with figure 7.

Figure 6(*e–h*) shows plots of Q_s *vs.* R_s in the four regions of the flow. The influence of the wall can be most clearly seen in figure 6(*e*); right at the wall the velocity gradients are, to first order,

$$A_{ij} = \begin{bmatrix} 0 & 0 & 0 \\ \partial u/\partial y & 0 & \partial w/\partial y \\ 0 & 0 & 0 \end{bmatrix} \tag{4.1}$$

which produces $Q_s = -[(\partial u/\partial y)^2 + (\partial w/\partial y)^2]/2$ and $R_s = 0$. This accounts for some of the shape of figure 6(*e*); the values of Q_s and R_s for the first few planes nearest the wall fell on vertical lines, with some of the highest dissipations of the flow. Moving away from the wall, an increasing preference for the rate of strain field to have unstable node/saddle/saddle topologies (intermediate principal strain rate positive) can be observed. There does not seem to be any particular preference for the set of ratios 3:1:–4 reported by Ashurst *et al.* (1987) (see figure 3); in the outer region of the flow it would appear that the ratios 1:1:–2 model the behaviour more closely.

The initially high, then decreasing influence of the wall can also be seen in the plots of $S_{ij}S_{ji}$ *vs.* $-\Omega_{ij}\Omega_{ji}$ in figure 6(*i–l*). The values for the mean flow would follow 45° lines and in the viscous sublayer this was closely true for all the points, as would be expected from a decomposition of (4.1) into symmetric and skew-symmetric parts.

The influence of the wall extended into the buffer layer but is not observed in the outer region (6*g*,*h*), where the PDFs closely resemble plots computed from other inhomogeneous shear flows (Sondergaard *et al.* 1991; Soria *et al.* 1994). The contours in the joint PDFs of the strain invariants (6*g*,*h*) show a characteristic, nearly straight line, shape similar to the mixing layer with turbulent initial conditions (Soria *et al.* 1994, figure 17). This appears to be associated with flow structures at intermediate scales with invariants which behave as $\gamma^3 + Q\gamma + R = 0$ where γ is the local real eigenvalue. Physically, this can be interpreted as a locally two-dimensional (tube-like) flow with an out-of-plane rate of strain (γ) which is approximately constant over the volume of the structures. This behaviour of the invariants associated with intermediate-scale motions is in contrast to nearly constant ratios of the principal rates of strain implied by (2.6) which seems to apply only to the finest-scale regions

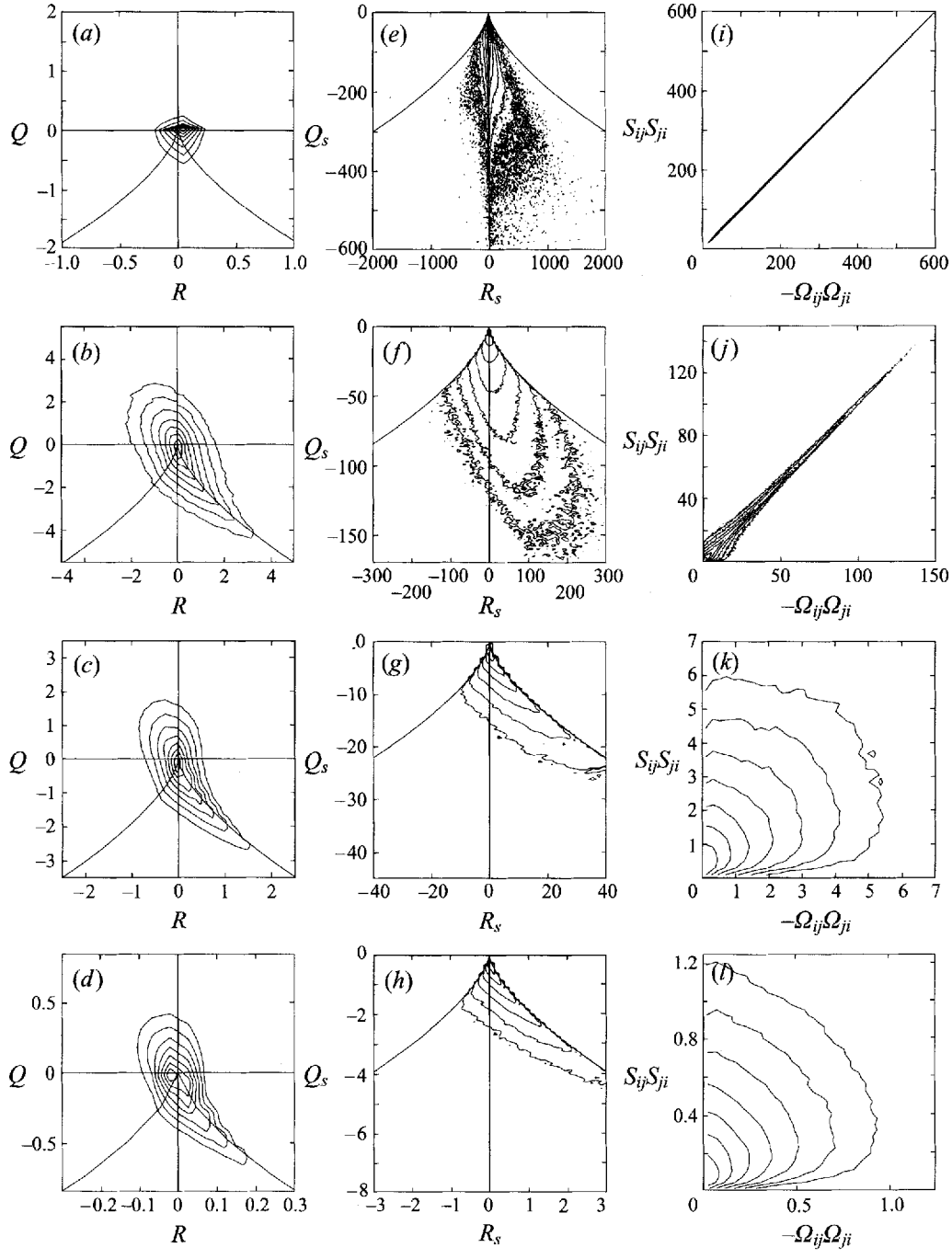

FIGURE 6. PDF plots of (*a–d*) Q *vs.* R, (*e–h*) Q_s *vs.* R_s, (*i–l*) $S_{ij}S_{ji}$, *vs.* $-\Omega_{ij}\Omega_{ji}$ in the four flow regions: viscous sublayer (*a*, *e*, *i*), buffer layer (*b*, *f*, *j*), log-law region (*c*, *g*, *k*), wake region (*d*, *h*, *l*). The plots show half-decade contours of relative frequency over a four-decade range. In the plots of Q *vs.* R and Q_s *vs.* R_s, the line $D = (27/4)R^2 + Q^3 = 0$ which divides the plane into regions where the tensor has purely real and complex-conjugate pair/real eigenvalues is shown as reference. Velocity gradients have been normalized by $\overline{U}_c/\delta$.

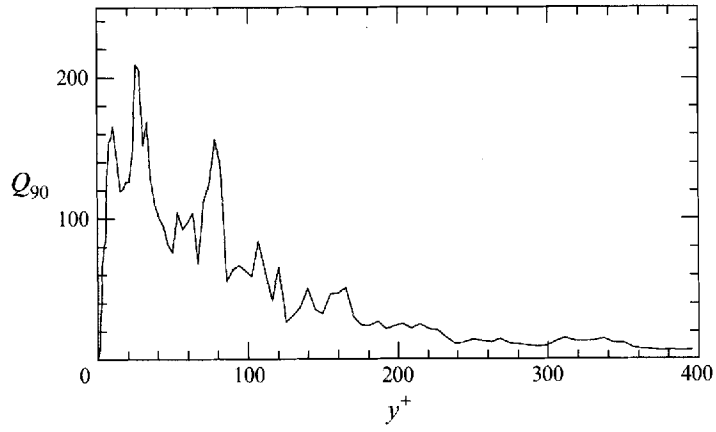

FIGURE 7. Plot of the 90th percentile of Q as a function of y^+ from one realization of the flow. Velocity gradients have been normalized by $\overline{U}_c/\delta$.

of the flow with the highest rates of dissipation. It is interesting that in the outer region, the PDFs indicate that pure rotational motion was rare. This is in contrast to the observations in the mixing layer by Chen *et al.* (1990) and Soria *et al.* (1994) where streamwise rib vortices were found to be in nearly solid-body rotation. This behaviour can also be noted in the buffer layer (close to the origin in figure 6*f*).

5. Results: flow structures

In order to gain an understanding of the spatial structure of the turbulence, a number of plots of flow field quantities were viewed interactively using a graphics workstation.

In figure 8 we present three views of a subset of the flow bounded below by the wall. In vertical extent, the subset reaches nearly to the centre of the channel; the dimensions in wall units are: $\Delta x^+ = 670$, $\Delta y^+ = 375$ and $\Delta z^+ = 640$. The view is from upstream and to the side of the box, near the wall.

In figure 8(*a*) the plot is of an iso-surface of enstrophy $-\Omega_{ij}\Omega_{ji}$. A number of tube-like structures can be seen, with a general inclination downstream and away from the wall. Since the highest mean-flow enstrophy occurs at the wall and drops to zero in the centre of the channel, the surface for the chosen level terminates above the wall. This characteristic of the flow also explains the distorted sheet-like shape of the surface near the wall: for the mean flow only one surface would be visible, a plane near and parallel to the wall; the perturbation enstrophy is apparently manifested as tube-like structures which begin near the wall and extend away from it, thus resulting in the appearance of an elastic sheet distorted by protruding tubes. Visualization of vortex lines confirmed that the tube-like shapes away from the wall contained vorticity aligned with the axes of the tubes. Very close to the wall, vortex lines extended in the spanwise (z) direction as expected.

The iso-surface plotted in figure 8(*b*) is of $S_{ij}S_{ji}$, proportional to the local viscous dissipation of kinetic energy. The contour level was the same as for the enstrophy in figure 8(*a*). Near the wall, the shape of the surface was very similar to that for the enstrophy, in agreement with the PDFs of figure 6(i,j). Away from the wall, high enstrophy and dissipation tended to occur in the same regions of space (on the scale of the length of the tube-like structures in figure 8*a*), but definite structure is less easy to discern.

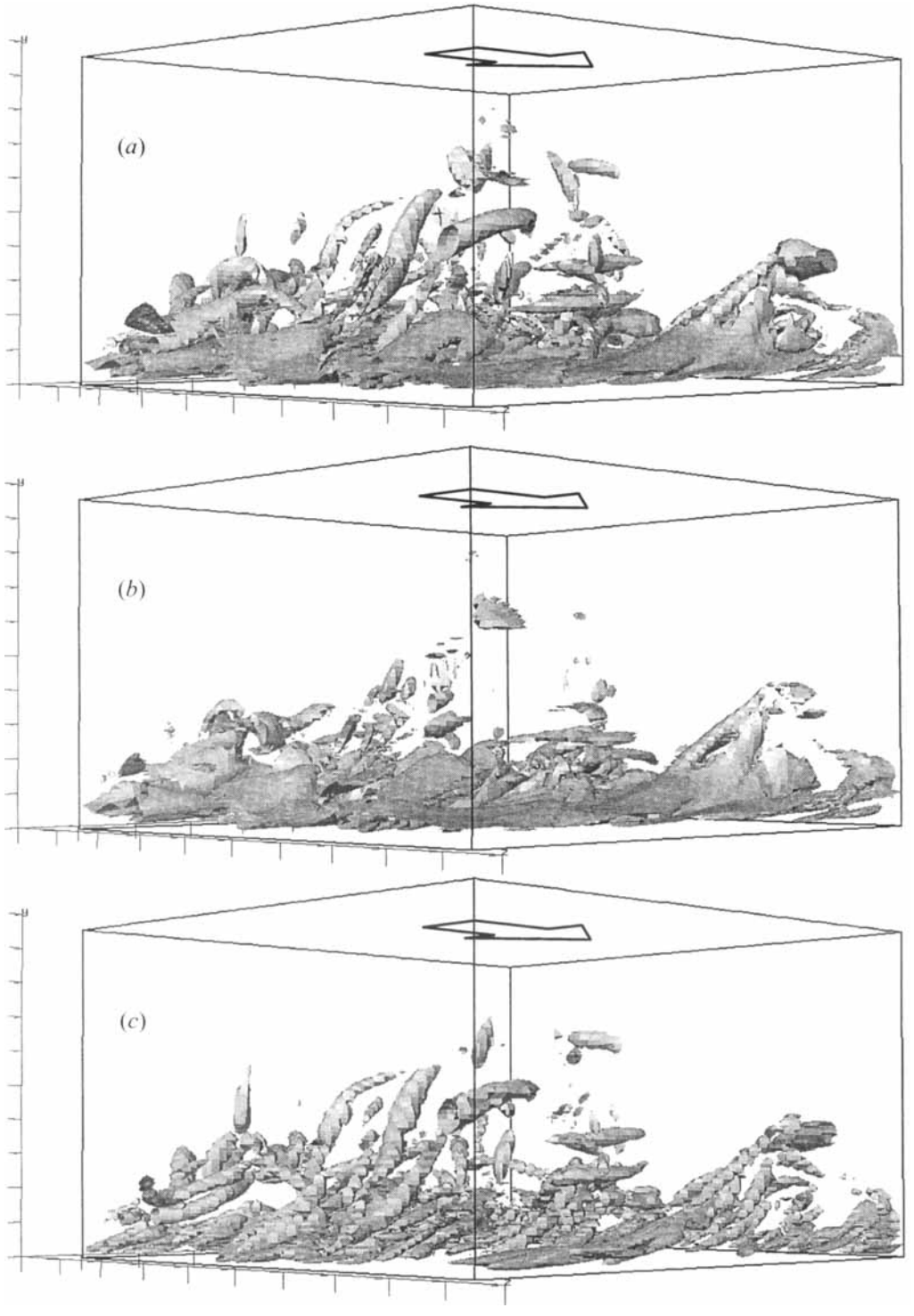

FIGURE 8. Flow visualization in subset of the flow bounded below by the wall. (*a*) iso-surfaces of enstrophy $-\Omega_{ij}\Omega_{ji}$, (*b*) iso-surfaces of viscous dissipation (proportional to $S_{ij}S_{ji}$), (*c*) iso-surfaces of discriminant D (for $R \leqslant 0$: intensity of stable focus/stretching topology). Box size in wall units: $\Delta x^+ = 670$, $\Delta y^+ = 375$ and $\Delta z^+ = 640$. Mean flow direction indicated by arrows.

In figure 8(*c*) we present a plot of flow structures which have strong stable focus/stretching topologies. More specifically, the plot is of an iso-surface of the discriminant $D = (27/4)R^2 + Q^3$ for which the third invariant of the velocity gradient tensor $R \leqslant 0$; this corresponds to a contour in the upper-left side of the (Q,R)-plane (see the contour lines in figure 1). The structures had tubular shapes; close to the wall the structures tended to lie parallel to it while away from the wall they tended to align with the most extensive mean principal strain rate direction (45°). At some distance from the wall, the structures with stable focus/stretching topology displayed a high degree of correspondence to the structures with large enstrophy shown in figure 8(*a*). We would like to emphasize, however, that the means of visualization employed here is significantly different to previous methods derived from the velocity or vorticity field alone. The flow structures revealed by the discriminant, which involves a balance between rotation and strain, are distinct from those obtained from contours of enstrophy or dissipation. This is particularly apparent in the wall region, where the discriminant reveals discrete structures. In fact, using this method, one can identify individual structures which begin very close to the wall and extend all the way to the middle of the channel.

A digression concerning the motivation for contour plots based on topological characteristics of the velocity gradient tensor is in order. Chen *et al.* (1990) demonstrated with two-dimensional plots based only on topological classification (i.e. the four classes shown in figure 1) that structures thus revealed were in many ways similar to those shown using more conventional scalar quantities such as enstrophy and in addition could reveal e.g. sites where vorticity was being stretched or compressed. That approach had utility for the flows they investigated, in which many features had large planar extent and could be dealt with easily using two-dimensional plots. In the channel flow, the turbulence is more strongly three-dimensional and three-dimensional contour plots based on classification alone are very difficult to visualize successfully since each point in space must belong to one of the four topological classes, meaning that a view of zero-threshold contours of any one topology may be of a very complex space-filling object. To overcome this difficulty, a scalar magnitude was needed which could be assigned to each flow classification and it was decided to use the discriminant D as a measure of intensity, since in a model based on the solution of a restricted Euler equation, the discriminant is a conserved quantity for fluid particles (see § 7). Hence the structures that are revealed are related to PDFs such as those of figure 6(*a–d*); points which lie above a contour of constant D in the second quadrant of a (Q,R)-diagram fall inside the structures with stable focus/stretching topology in figure 8(*c*). In this way spatial information which is absent in the PDFs may be recovered. Intensities based simply on radius from the origin in (Q,R)-space revealed the same structures but with slightly different shapes. On the other hand, a visualization method that is not based on computed contour surfaces (e.g. a pointwise or 'fog' plot) might reveal similar three-dimensional structures based on topological classification alone: we have not attempted to use such a method here.

Figure 9 presents different views of the structures seen in figure 8(*c*). Figure 9(*a*) is a view from above and slightly downstream of the region which again emphasizes the fact that each of the structures tended to be a separate entity. Figure 9(*b*) is a view across the flow at wall level, which shows that the structures did not reach to the wall but that those nearest the wall originated in the buffer layer; as in figure 9(*a*) the change in alignment from streamwise near the wall towards the most extensive mean principal strain rate direction can be clearly seen. In figure 9(*b*) the structures

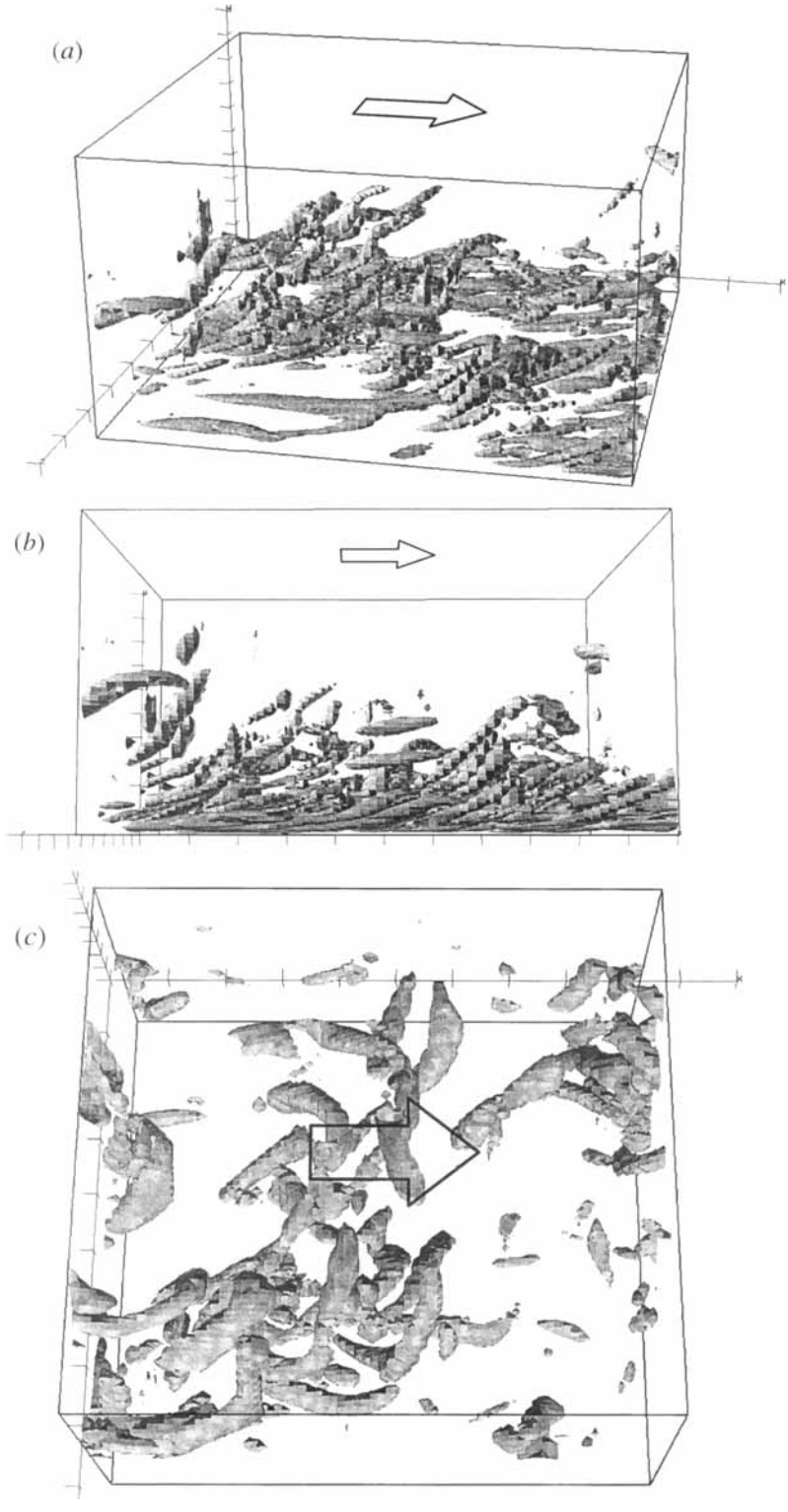

FIGURE 9. View of structures with stable focus/stretching topologies shown in figure 8(*c*), looking: (*a*) from above and downstream, (*b*) spanwise along the wall, (*c*) from above (this last view shows only structures in the outer regions of the flow, using a lower contouring level than in *a* and *b*).

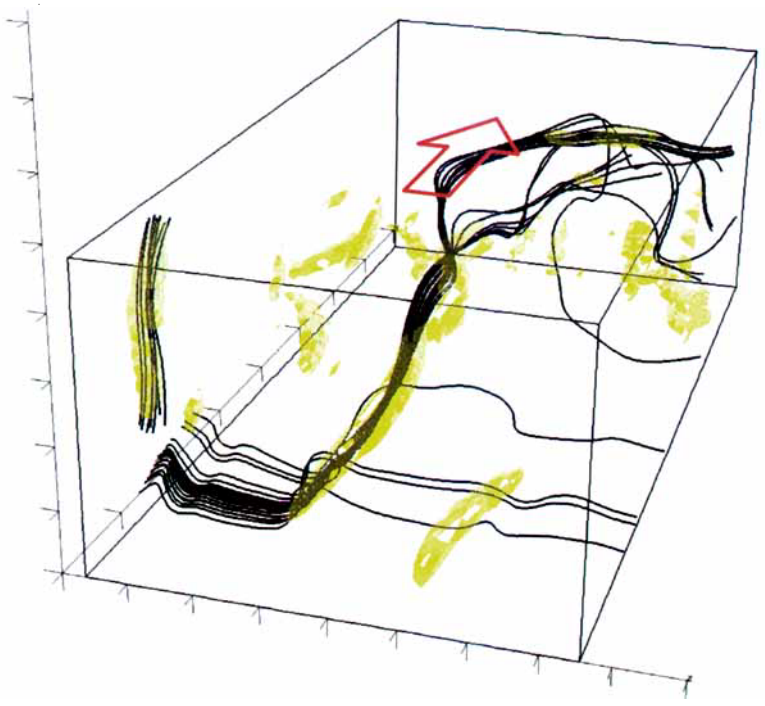

FIGURE 10. Structures with stable focus/stretching topology (shaded yellow) showing vortex lines which run through selected cores. Box size in wall units: $\Delta x^+ = 590$, $\Delta y^+ = 190$ and $\Delta z^+ = 285$.

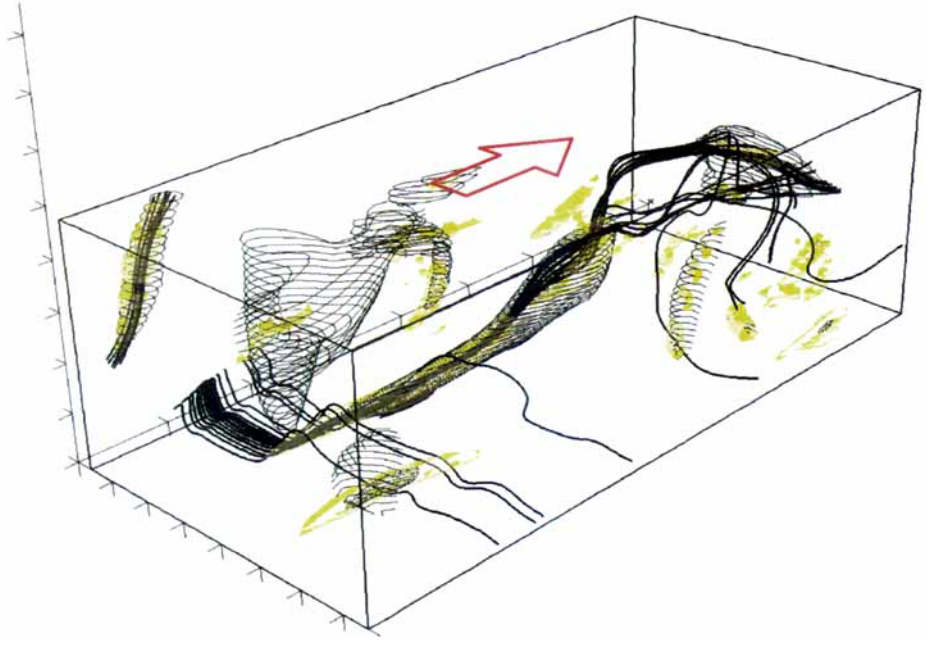

FIGURE 11. Structures with stable focus/stretching topology showing vortex lines which run through the cores, together with overlay of contours of a low-pressure isosurface (thin contour lines parallel to wall). Data set is the same as for figure 10.

seem to disappear at about the beginning of the wake region, which was largely a consequence of the contour level of D chosen for the plot, since at a lower value the structures may be observed at the centre of the channel.

To illustrate the shape of the structures near the centre of the channel, we present in figure 9(*c*) a view of structures with stable focus/stretching topologies in the top of the same region as chosen for figures 8, 9(*a*) and 9(*b*), looking towards the wall. The contour level was set at a lower value than for the previous figures and contours were only drawn in the top two-thirds of the region to prevent confusion with structures nearer the wall. This shows that, in the outer region of the flow, the structures tended to obtain a spanwise orientation.

As a consequence of the similarity between structures with stable focus/stretching topologies and structures with high enstrophy in regions away from the wall (figure 8*a*, *c*), it might be expected that the structures shown in figures 8(*c*) and 9 would contain aligned vorticity undergoing stretching. Indeed this was most often the case. To illustrate this, we concentrate in figure 10 on a smaller subset of the flow than previously shown (in fact, a subset of the space shown in figures 8 and 9). An iso-contour of D for stable focus/stretching topologies is shown as a translucent yellow surface. In addition to the surfaces are shown (thick) vortex lines which were chosen to run through two of the structures, one near to and predominantly parallel to the wall, the other inclined at nearly 45° to it. The lines were obtained by releasing particle traces in the vorticity field near the axes of these two structures and integrating up and downstream. It is evident that the vortex lines tended to be well-aligned and tightly bunched within the two structures, with divergence of the lines associated with a breakdown of the structure nearly aligned with the wall.

Another view of this region is shown in figure 11, where we have also overlaid contours corresponding to an iso-surface of low pressure (thin lines parallel to the wall). It may be seen that the two structures in which the vortex traces were released were also regions of low pressure. The correspondence between the shapes of structures was often observed in other regions of the flow, but was not universal.

6. Results: vorticity alignment

A feature revealed in previous investigations of turbulent flows (Ashurst *et al.* 1987; Sondergaard *et al.* 1991; Vincent & Meneguzzi 1991; Tsinober *et al.* 1992; Vincent & Meneguzzi 1994) has been the tendency for alignment between the intermediate principal strain rate direction and the vorticity, particularly at sites of high viscous dissipation of kinetic energy. This alignment has been described as a kinematic effect by Jimenez (1992). A similar kinematic alignment should occur near the wall in boundary layer flows since on average the most extensive principal strain rate points downstream, away from the wall at 45° and the most compressive principal strain rate points downstream, towards the wall at 45°, leaving the intermediate principal strain rate direction to align spanwise with the average vorticity.

We present in figure 12 estimates of the PDFs of the angle made between the local vorticity $\boldsymbol{\omega}$ and the three principal strain rate directions $\boldsymbol{e}_1$, $\boldsymbol{e}_2$, $\boldsymbol{e}_3$ (θ_1, θ_2 and θ_3) for all points in each of the four regions of the flow. While figure 12(*a*) displays the expected alignment effect, with the density for θ_2 peaking near zero angle, the remaining plots show that the probability density dropped towards zero at an angle of zero, with the effect being most marked in the outer region of the flow.

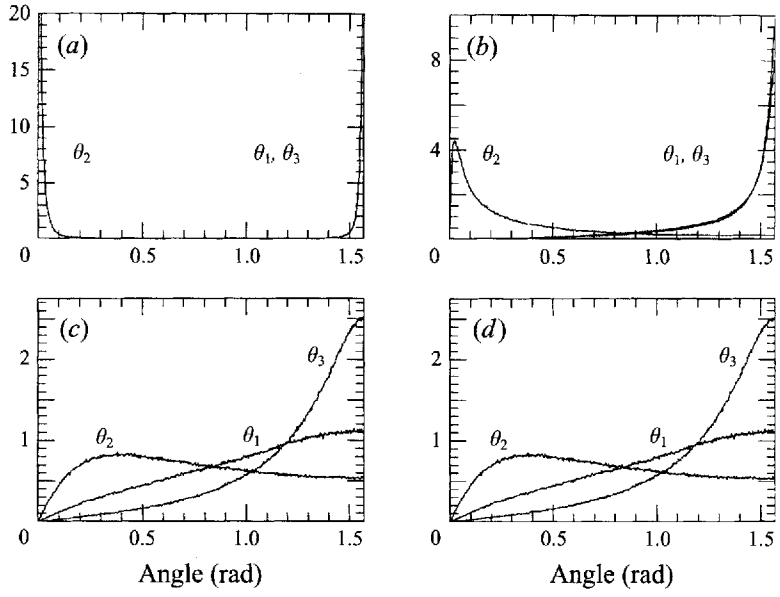

FIGURE 12. Probability density function (PDF) estimates for the angle made between the vorticity and the principal strain rate directions. (*a*) viscous sublayer, (*b*) buffer layer, (*c*) log-law region, (*d*) wake region.

These results may seem at variance with previous numerical and experimental investigations in that they seem to indicate a forced slight misalignment between the vorticity and the intermediate principal rate of strain direction. This feature, of probability densities falling to zero, is, however, a consequence of the computation of probability densities of angle, rather than cosine of angle (R. Sondergaard 1994, private communication). If one is interested in the probabilistic properties of the alignments of two vectors, one, e.g. the vorticity, with given fixed direction, and the other with random orientation, then the lengths of the vectors are clearly irrelevant and both may be normalized to unity. Then the given vector may be fixed with one end at the origin and considered to point along a coordinate axis; if the random vector also has one end fixed at the origin, the probability density of finding its other end at any point on the unit sphere is uniform (value: $1/4\pi$). Using this spherical geometry and elementary calculus, it may be shown that the probability density of the angle θ between the given vector and the random vector is $\sin\theta$ ($0 \leqslant \theta < \pi/2$) while the probability density of the cosine of θ is constant at $1/2$ ($-1 \leqslant \cos\theta < 1$). Thus the fall in values of probability density of θ_2 in figure 12(*b*,*c*) near zero angle is an indication of a slight randomness in the orientation of the intermediate principal strain rate direction with respect to the vorticity, rather than forced misalignment. The issue of weighting effects inherent in PDFs of transformed variables has also been raised by Lund & Rogers (1994) in discussion of functions of the intermediate principal rate of strain λ_2.

In figure 13 we present, as an alternative to figure 12, PDFs of the cosine of the angle made between the local vorticity $\boldsymbol{\omega}$ and the three principal strain rate directions $\boldsymbol{e}_1$, $\boldsymbol{e}_2$, $\boldsymbol{e}_3$ (θ_1, θ_2 and θ_3). The high preference for alignment of the vorticity with the intermediate principal rate of strain direction is shown by the large deviation of the PDF for θ_2 from the value of $1/2$ near cosines of ± 1. This preference is apparently a robust feature of turbulent flows in general, and is reinforced near the walls by the boundary conditions of this flow.

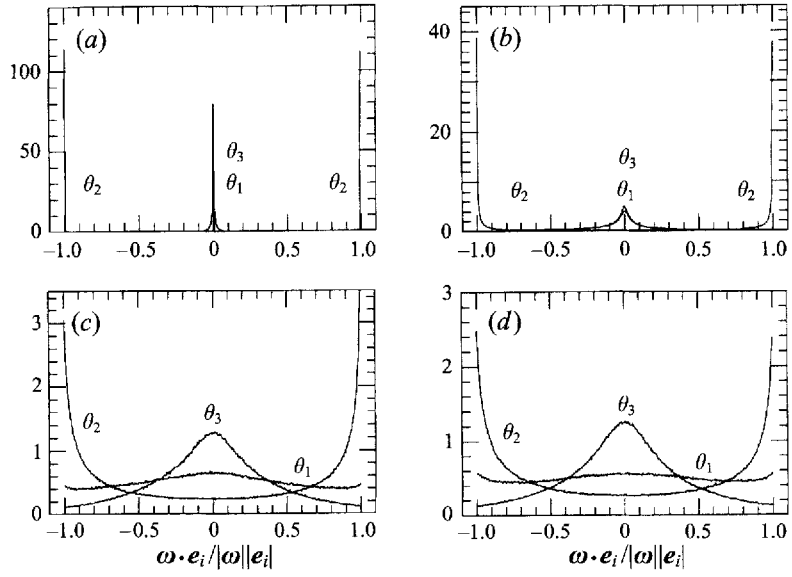

FIGURE 13. Probability density function (PDF) estimates for the cosine of the angle made between the vorticity and the principal strain rate directions. (*a*) viscous sublayer, (*b*) buffer layer, (*c*) log-law region, (*d*) wake region.

7. Discussion

The results obtained here are of particular interest in the way they are related to results obtained in simulations of other turbulent flows and visualization of boundary layer flows.

Of considerable significance is the prospect of finding universal features of fine-scale motions in turbulent flows. Recent investigations of simulations of driven isotropic turbulence (Ashurst *et al.* 1987; She *et al.* 1990; Vincent & Meneguzzi 1991; Ruetsch & Maxey 1991) have indicated a number of common features which we summarize as follows. The most intense vorticity is concentrated in tube-like structures with lengths of the order of the integral scale of the flow and typical diameters intermediate between the Taylor and Kolmogorov microscales. Most of the viscous dissipation in the flow occurs in annular regions surrounding the tubes and in these regions the intermediate principal strain rate is positive and aligned with the vorticity (tube axis), indicating stretching of the vorticity in the tubes. She *et al.* found that intermediate levels of vorticity tended to be organized in sheet-like structures. Vincent & Meneguzzi (1994) have indicated that the vortex tubes form by the rolling up of vortex sheets which themselves evolve from pancake-like regions of high strain rate.

Our results (e.g. figure 8*a*) show that away from the wall, regions of intense vorticity in the channel flow tended also to be organized into tubular-shaped structures with x,y alignments which ranged in direction from 0° to 45° to the wall (45° being the extensive principal strain rate direction of the mean flow). Significant z-components of alignment could also be observed (consistent with the existence of vortex loops), particularly further from the wall, although no evidence of a full loop or ring was found in the plots of surfaces of iso-enstrophy. The tubular shapes became less easy to discern close to the wall since there the most intense vorticity tends to be directed spanwise, parallel to the wall. PDFs of the second and third invariants of

the rate of strain tensor (figure 6*i–l*) show that the intermediate principal strain rate tended to be positive when viscous dissipation was high at sites away from the wall. These features indicate a degree of similarity at small scales between the structures observed in driven isotropic turbulence simulations and the outer regions of the channel flow.

While some explanations for the tendency for alignment between the intermediate principal strain rate direction and vorticity have been advanced on a kinematic basis (e.g. Jimenez 1992), dynamical models have also produced this result. The transport equation for the evolution of the velocity gradient tensor $\boldsymbol{A}$ in incompressible flow is

$$\frac{\mathrm{d}A_{ij}}{\mathrm{d}t} + A_{ik}A_{kj} - \tfrac{1}{3}(A_{mn}A_{nm})\delta_{ij} = H_{ij}, \tag{7.1}$$

where

$$H_{ij} = -\left(\frac{\partial^2 p}{\partial x_i \partial x_j} - \frac{\delta_{ij}}{3}\frac{\partial^2 p}{\partial x_k \partial x_k}\right) + \nu\frac{\partial^2 A_{ij}}{\partial x_k \partial x_k} \tag{7.2}$$

is a term which links the evolution of the velocity gradient tensor for a fluid particle to the surrounding flow through cross-derivatives of the pressure field and viscous diffusion.

Setting $\boldsymbol{H} = 0$ converts (7.1) into a system of ODEs which will be referred to as the Restricted Euler equations. These equations describe the evolution of the components of $\boldsymbol{A}$ for a particle moving in the absence of any influence from nearby particles though the pressure–viscous diffusion term. The only effect of the surroundings is that imposed by continuity. The behaviour of this system has been studied and it was given linearized, then asymptotic solutions by Vieillefosse (1982, 1984). Subsequently the Restricted Euler equations were solved exactly by Cantwell (1992). In this solution, the second and third invariants R and Q evolve along a trajectory of constant D in the (Q,R)-plane (see figure 1), with R increasing as time proceeds. The invariants and the various components of $\boldsymbol{A}$ become singular in finite time for all initial conditions apart from those on the trajectory which leads to the origin, in which case the components of $\boldsymbol{A}$ become singular as Q and R approach zero. The interesting feature of the Restricted Euler system is that as the solution evolves towards singularity, the geometry of the gradient tensor is such that the intermediate principal strain rate is positive and the vorticity is exactly aligned with the intermediate principal strain rate direction. In this model, the vorticity alignment is inherent in the dynamics of a single particle.

PDFs of Q *vs.* R (figure 6*a–d*) show a number of similarities with scatter plots prepared from inhomogeneous shear flow simulations, with the most obvious common feature being the observed preference for stable focus/stretching and unstable node/saddle/saddle topologies. Unstable node/saddle/saddle topologies tended to have low values of the discriminant D. In general, there is a tendency for Q and R to lie in a roughly elliptical region near the origin, with a branch extending into the lower-right quadrant. While at this stage there is no full theoretical explanation for these trends, they are consistent with behaviour predicted by the Restricted Euler model (Cantwell 1992) and its extension to the $\boldsymbol{H} \neq 0$ case (Cantwell 1993).

The use of flow visualization based on invariants of the velocity gradient tensor $\boldsymbol{A}$ provides a new and unambiguous means for identifying flow structures based directly on the velocity field, whereas in many other methods the structures observed depend on the frame of reference of the observer. The invariants Q and R (but not Q_s, R_s or Q_Ω) are also invariant under affine transformations of the velocity field. The flow visualization based on structures with stable focus/stretching topologies (figures 8*c*,

9–11) provides some interesting evidence of direct linkage between the inner and outer regions of the flow, with structures which originate at the outer edge of the viscous sublayer and extend through the log-law layer in some instances to the outer wake region.

Many, if not all, of the observed structures seem likely to be associated with hairpin or horseshoe vortices (note e.g. the similarity between figure 10 here and figure 20 of Kim & Moin 1986, observed at a lower Reynolds number). A more extensive study of the relationship between the structures and vortex lines is needed to establish this conclusively. The apparent lack of observations of full loops of stable focus/stretching topology reaching from the wall region out into the outer region and back to the wall could be a consequence of either the thresholding obtained by plotting only surfaces of one value of D or a change in topological classification e.g. to unstable focus/compressing along the axis of the vortex lines. The lack of such symmetrical features is to be expected in turbulent boundary layer flows of moderate to high Reynolds numbers, as discussed by Smith *et al.* (1991).

The observed close relationship between structures with stable focus/stretching topology and elongated regions of low-pressure is given added significance by the finding of Robinson, Kline & Spalart (1988) that elongated low-pressure regions corresponded with 'vortical structures' in boundary layers. The implication is that such features may also be located by searching for regions of stable focus/stretching topology. We note the apparent similarity between the general shape of the structures shown in figures 8–10 here and those presented in a sketch of 'vortical structure populations' by Robinson (1991, figure 13*a*).

The relationship to flow visualization based in physical, rather than numerical experiments is not easy to establish, but we also note the apparent similarity between the observations of structures of stable focus/stretching topology made here and the experimental results of Head & Bandyopadhyay (1981) obtained in zero-pressure-gradient smoke tunnels. Their observations suggested that the predominant boundary layer feature was structures formed from groups of hairpin vortices or stretched vortex loops 'substantially straight over a large portion of their length and inclined to the surface at a characteristic angle of something like 45°'. They suggested in addition that longitudinal vortex pairs which they observed formed in the wall layers were likely to be associated with the hairpin vortices observed in the outer region. Our results support this suggestion, since it can be observed in figure 9(*a*,*b*) that many of the structures begin in the wall region, almost parallel to the wall, before turning out into the main flow. Further experimental evidence for this change in characteristic angle of structures when moving from the inner to the outer region of the flow has recently been presented by Jovic (1993).

In the 'attached eddy' model for wall turbulence first proposed by Townsend (1976) and subsequently developed by Perry and co-workers (e.g. Perry & Chong 1982; Perry, Li & Marušić 1991; Perry, Marušić & Li 1994), turbulence statistics for the boundary layer are calculated on the assumption that the turbulence can be modelled by a random array or hierarchy of geometrically similar eddies. The basic features of characteristic 'Λ' vortices assumed in the later versions of the model are as follows: vortices originate in the buffer layer and leave two long tails in this zone; the two legs which form the Λ shape protrude into the turbulent wall region are inclined at approximately 45° to the mean velocity and lean downstream. The distance between the two tails of the vortex follows the Kline scaling of approximately 100 wall units. In broad terms the above description is in agreement with the shapes and distribution of structures seen in our figures 8–10. Since the channel half-width here is 395 wall

units, an extensive hierarchy of scales is not to be expected; however the range of scales should increase with Reynolds number. The apparent qualitative agreement encourages a review of the assumptions and predictions of the attached model in relation to the present simulation results.

8. Conclusions

Probability density functions of tensor invariants for the outer regions of the channel flow showed a similarity to other turbulent flows with apparent preference for stable focus/stretching and unstable node/saddle/saddle topologies. At sites of high viscous dissipation of kinetic energy, the intermediate principal strain rate was positive, becoming more positive, closer to the most extensive principal strain rate, away from the wall.

A novel visualization method, based on thresholding on the discriminant of the velocity gradient tensor and on the sign of its third invariant, was employed to show structures with stable focus/stretching topology. This method revealed arrays of discrete tube-like structures connecting the buffer layer with the outer region of the flow. In the wall region, the structures were nearly parallel to the wall, acquiring characteristic directions near 45° to the wall followed by a spanwise orientation at their outer limit in the outer region.

Study of the probability density of angle between the intermediate principal strain rate direction and the vorticity showed that the two directions tended towards alignment, as reported in previous studies of other turbulent flows. We have discussed a theoretical framework within which the dynamics of such effects may be investigated.

We would like to thank John Kim, Center for Turbulence Research, for making the results of the channel flow simulation available to us. Thanks also to Rolf Sondergaard, Stanford University, for pointing out the features of alignment PDFs, and to Julio Soria, Monash University, for making the source of figure 2 available to us.

The first author would like to thank the Department of Aeronautics and Astronautics, Stanford University, and The Center for Turbulence Research for their support during a period of leave from Monash University. Additional financial support was provided by ONR Grant N00014-90-J-1976 and the Stanford-Ames Joint Institute for Aeronautics and Acoustics.

REFERENCES

Antonia, R.A., Kim, J. & Browne, L.W.B. 1991 Some characteristics of small-scale turbulence in a turbulent duct flow. *J. Fluid Mech.* **233**, 369–388.

Antonia, R.A., Teitel, M., Kim, J. & Browne, L.W.B. 1992 Low-Reynolds-number effects in a fully developed turbulent channel flow. *J. Fluid Mech.* **236**, 579–605.

Ashurst, W.T., Kerstein, A.R., Kerr, R.M. & Gibson, C.H. 1987 Alignment of vorticity and scalar gradient with strain rate in simulated Navier–Stokes turbulence. *Phys. Fluids* **30**, 2343–2353.

Cantwell, B.J. 1992 Exact solution of a restricted Euler equation for the velocity gradient tensor. *Phys. Fluids* A **4**, 782–793.

Cantwell, B.J. 1993 On the behaviour of velocity gradient tensor invariants in direct numerical simulations of turbulence. *Phys. Fluids* A **5**, 2008–2013.

Chen, J.H., Chong, M.S., Soria, J., Sondergaard, R., Perry, A.E., Rogers, M., Moser, R. & Cantwell, B.J. 1990 A study of the topology of dissipating motions in direct numerical simulations of time developing compressible and incompressible mixing layers. In *Proc. Center for Turbulence Research 1990 Summer Program*, pp. 141–164. Center for Turbulence Research, Stanford, CA.

CHONG, M.S., PERRY, A.E. & CANTWELL, B.J. 1990 A general classification of three-dimensional flow fields. *Phys. Fluids* A **2**, 765–777.

HEAD, M.R. & BANDYOPADHYAY, P. 1981 New aspects of turbulent boundary-layer structure. *J. Fluid Mech.* **107**, 297–338.

JIMENEZ, J. 1992 Kinematic alignment effects in turbulent flows. *Phys. Fluids* A **4**, 652–654.

JOVIC, S. 1993 Two-point correlation measurements in a recovering turbulent boundary layer. In *Near-Wall Turbulent Flows* (ed. R.M.C. So, C.G. Speziale & B.E. Launder), pp. 921–930. Elsevier

KIM, J. 1989 On the structure of pressure fluctuations in simulated turbulent channel flow. *J. Fluid Mech.* **205**, 421–451.

KIM, J. & ANTONIA, R.A. 1993 Isotropy of the small scales of turbulence at low Reynolds numbers. *J. Fluid Mech.* **251**, 219–238.

KIM, J. & MOIN, P. 1986 The structure of the vorticity field in turbulent channel flow. Part 2. Study of ensemble-averaged fields. *J. Fluid Mech.* **162**, 339–363.

KIM, J., MOIN, P. & MOSER, R. 1987 Turbulence statistics in fully developed channel flow at low Reynolds number. *J. Fluid Mech.* **177**, 133–166.

LUND, T.S. & ROGERS, M.M. 1994 An improved measure of strain rate probability in turbulent flows. *Phys. Fluids* **6**, 1838–1847.

PERRY, A.E. & CHONG, M.S. 1982 On the mechanism of wall turbulence. *J. Fluid Mech.* **119**, 173–217.

PERRY, A.E. & CHONG, M.S. 1987 A description of eddying motions and flow patterns using critical point concepts. *Ann. Rev. Fluid Mech.* **19**, 125–155.

PERRY, A.E., LI, J.D. & MARUŠIĆ, I. 1991 Towards a closure scheme for turbulent boundary layers using the attached eddy hypothesis. *Phil. Trans. R. Soc. Lond.* A **336**, 67–79.

PERRY, A.E., MARUŠIĆ, I. & LI, J.D. 1994 Wall turbulence closure based on classical similarity laws and the attached eddy hypothesis. *Phys. Fluids* **6**, 1024–1035.

ROBINSON, S.K. 1991 Coherent motions in the turbulent boundary layer. *Ann. Rev. Fluid Mech.* **23**, 601–639.

ROBINSON, S.K., KLINE, S.J. & SPALART, P.R. 1988 Quasi-coherent structures in the turbulent boundary layer: Part II. Verification and new information from a numerically-simulated boundary layer. In *Near-Wall Turbulence* (ed. S.J. Kline & N.H. Afgan), pp. 218–247. Hemisphere.

RODI, W. & MANSOUR, N.N. 1993 Low Reynolds number k–ϵ modelling with the aid of direct simulation data. *J. Fluid Mech.* **250**, 509–529.

RUETSCH, G.R. & MAXEY, M.R. 1991 Small-scale features of vorticity and passive scalar fields in homogeneous isotropic turbulence. *Phys. Fluids* A **3**, 1587–1597.

SHE, Z.-S., JACKSON, E. & ORSZAG, S.A. 1990 Intermittent vortex structures in homogeneous isotropic turbulence. *Nature* **344**, 226–228.

SMITH, C.R., WALKER, J.D.A., HAIDARI, A.H. & SOBRUN, U. 1991 On the dynamics of near-wall turbulence. *Phil. Trans. R. Soc. Lond.* A **336**, 131–175.

SONDERGAARD, R., CHEN, J.H., SORIA, J. & CANTWELL, B.J. 1991 Local topology of small scale motions in turbulent shear flows. In *Proc. Eighth Symposium on Turbulent Shear Flows (Munich, September)*.

SORIA, J., SONDERGAARD, R., CANTWELL, B.J., CHONG, M.S. & PERRY, A.E. 1994 A study of the fine-scale motions of incompressible time-developing mixing layers. *Phys. Fluids* **6**, 871–884.

TOWNSEND, A.A. 1976 *The Structure of Turbulent Shear Flow*. Cambridge University Press.

TSINOBER, A., KIT, E. & DRACOS, T. 1992 Experimental investigation of the field of velocity gradients in turbulent flows. *J. Fluid Mech.* **242**, 169–192.

VIEILLEFOSSE, P. 1982 Local interaction between vorticity and shear in a perfect incompressible fluid. *J. Phys. Paris* **43**, 837–842.

VIEILLEFOSSE, P. 1984 Internal motion of a small element of fluid in an inviscid flow. *Physica* **125**A, 150–162.

VINCENT, A. & MENEGUZZI, M. 1991 The spatial and statistical properties of homogeneous turbulence. *J. Fluid Mech.* **225**, 1–20.

VINCENT, A. & MENEGUZZI, M. 1994 The dynamics of vorticity tubes in homogeneous turbulence. *J. Fluid Mech.* **258**, 245–254.

ZANG, T. A. 1991 Numerical simulation of the dynamics of turbulent boundary layers: perspectives of a turbulence simulator. *Phil. Trans. R. Soc. Lond.* A **336**, 95–102.

ZANG, T. A., KRIST, S. E. & HUSSAINI, M. Y. 1989 Resolution requirements for numerical simulations of transition. *J. Sci. Comput.* **4**, 198–217.